




# Iron oxide nanoparticles–cellulose: a comprehensive insight on nanoclusters formation

Leonardo Zanata<sup>1</sup>, Aryane Tofanello<sup>2</sup>, Herculano S. Martinho<sup>1</sup>, José A. Souza<sup>2</sup>, and Derval S. Rosa<sup>1,\*</sup> 

<sup>1</sup> Center for Engineering, Modeling, and Applied Social Sciences-CECS, Universidade Federal Do ABC (UFABC), São Paulo 09210-580, Brazil

<sup>2</sup> Center for Natural and Human Sciences-CCNH, Universidade Federal Do ABC (UFABC), São Paulo 09210-580, Brazil

Received: 28 April 2021

Accepted: 25 September 2021

Published online:

3 January 2022

© The Author(s), under exclusive licence to Springer Science+Business Media, LLC, part of Springer Nature 2021

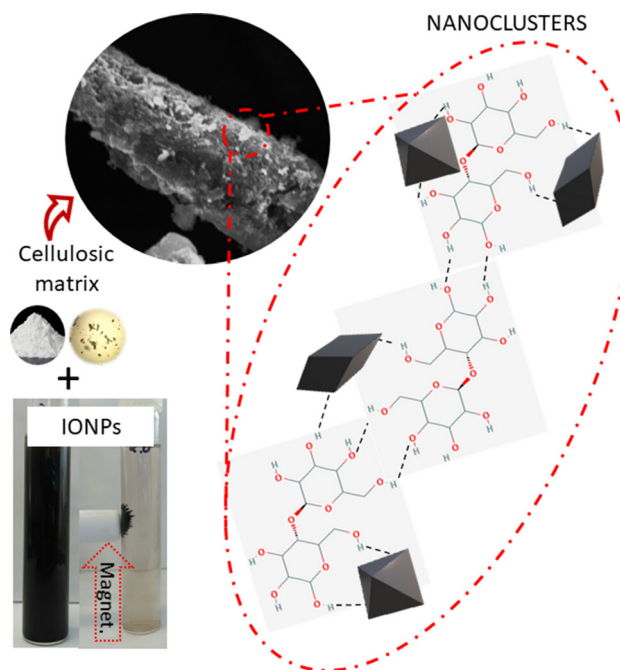
## ABSTRACT

Due to unique nanoscale properties, as superparamagnetism, iron oxide nanoparticles (IONPs) hybridized with cellulosic matrixes are an attractive material for environmental purposes. Previous studies obtained IONPs–cellulose clusters by the coprecipitation route. Nevertheless, the forces which bind IONPs and cellulosic matrixes and allow the nanocluster formation have not been well described. This study investigated the nanoclustering formation of superparamagnetic (SPM) IONPs and cellulosic materials. IONPs nanoclusters and hybrids were coprecipitated with microcrystalline cellulose (MC) in mass proportions of 1:0.5, 1:2, and 1:8. Lignocellulosic residues (LR) were also used as an organic matrix in mass proportions of 1:2. Dynamic light scattering analyses revealed that the obtained IONPs–organic clusters present sizes between  $1.46 \pm 0.49$  and  $6.84 \pm 3.15$   $\mu\text{m}$ . The MC and LR organic matrix size were decisive for the hybrids' final cluster size. Scanning electron microscopy images of the materials show an irregular morphology due to particle aggregation, while hybrids showed fibril character and the presence of crystal IONPs deposition at their surfaces. Micro-Raman spectra showed assignments of hematite ( $\alpha\text{-Fe}_2\text{O}_3$ ), goethite ( $\alpha\text{-FeOOH}$ ), magnetite ( $\text{Fe}_3\text{O}_4$ ), and wustite ( $\text{FeO}$ ), as a result of the coprecipitation process. Magnetization assays showed that the obtained clustered hybrids present SPM behavior at room temperature, despite to the cellulosic backbone presence and size. X-ray photoelectron spectroscopy brings light over the nanoclusters surface binding energies, evidencing the hydrogen bonding of the IONPs over the hydroxyl groups of MC and LR, clarifying the nanoclustering formation among heterogeneous IONPs and cellulosic matrixes.

Handling Editor: Dale Huber.

Address correspondence to E-mail: dervalrosa@yahoo.com.br; derval.rosa@ufabc.edu.br

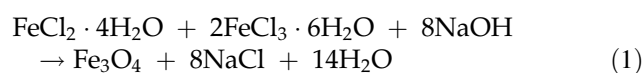
## GRAPHICAL ABSTRACT



## Introduction

Iron oxide nanoparticles (IONPs) present unique properties such as superparamagnetic (SPM) behavior at room temperature, zero coercive field, chemical stability, low toxicity, and formation of magnetic monodomains, due to its nanometric scale. These properties are attractive due to their biological and environmental potential applications [1–4]. In the environmental field, especially in wastewater treatment, their physical–chemical properties are useful in the direct and indirect removal of toxic pollutants, due to their high surface area and aspect ratio [4–6]. Superparamagnetic (SPM) iron oxides, such as magnetite, may be obtained through coprecipitation, a widely applied method due its simplicity, low cost, and efficiency [4, 6, 7]. Magnetite preparation process follows the stoichiometry indicated in Eq. 1 [8]. Excess of hydroxyl groups (1:2:8 stoichiometry) is

commonly used during hydrothermal synthesis by coprecipitation, aiming to avoid competition for other iron oxide phases. Consequently, nanosized iron oxides shall cluster after their formation, since the nanocrystals assembled into submicron dimensions [8] tending to form dipolar interactions [9], leading to active area loss and, in some cases, nanoparticles fast precipitation [5].



On the other hand, this method also allows the hybridization of the inorganic IOs with organic material. Hybridization renders better biocompatibility, biodegradability as well as structured aggregation of the end material [10–12]. In this scenario, a clustering structure-controlled formation is advantageous in order to increase the hybrids surface area [5], while numerous smaller-sized nanocrystals

bound together (nanoclusters) in the organic backbone structure (micro scale), keeping its saturation magnetization and, therefore, its superparamagnetic features [2, 4–6]. This nanoclustering assembling of IONPs can produce secondary structures, which possess a higher saturation magnetization value, while retaining the original superparamagnetic behavior of their primary nanoparticle constituents, even if its overall cluster size exceeds the SPM critical size at room temperature [3, 8].

Micro and nanostructures of cellulose were already applied as IONPs base structures. During the coprecipitation of IONPs with cellulose, the newly formed particles deposit on the surface of the cellulosic matrix, which will precipitate as hybrids [10–14]. The abundant presence of hydroxyl groups on the surface of the cellulosic matrix, in association with an acidic medium formed by iron salts ions, suggests that hydrogen bonds are formed between both phases during the coprecipitation process. Previous characterization [5, 6, 10–12] was made in IONPs/cellulosic hybrids. However, those works focused mainly on the presence of both organic and inorganic phases on the produced end materials, paying minor attention to mechanism which binds the inorganic and the organic phases.

This study aims to investigate superparamagnetic IONPs and cellulose nanoparticles obtention by coprecipitation, seeking to elucidate the nanoclustering binding process during these materials' hybridization. Assays of dynamic light scattering (DLS), scanning electron microscopy (SEM), Fourier-transformed infrared spectroscopy (FTIR), micro-Raman spectroscopy, X-ray photoelectron spectroscopy (XPS), and magnetization were carried out.

## Materials

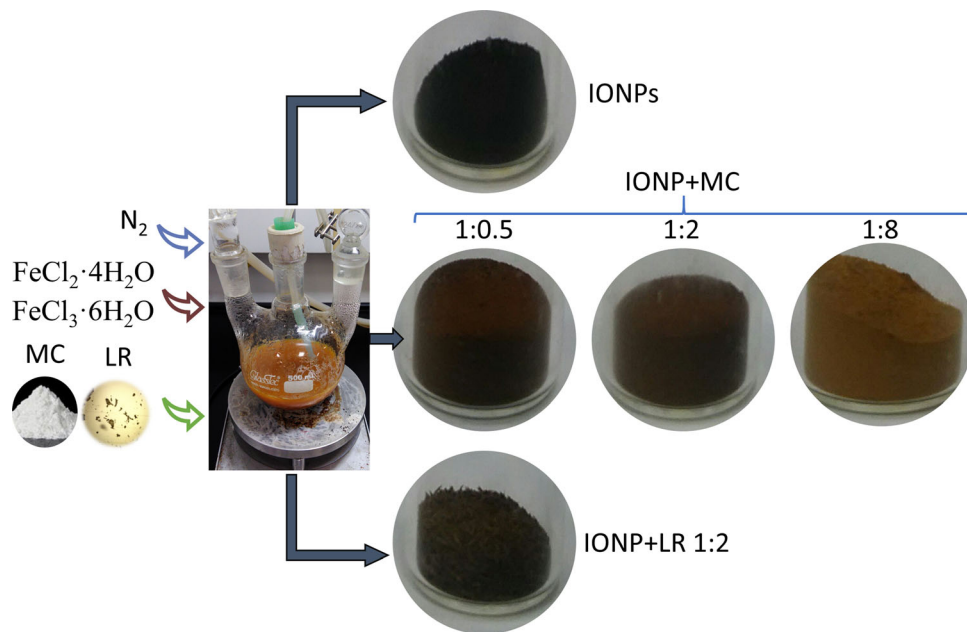
Ferrous chloride ( $\text{FeCl}_2 \cdot 4\text{H}_2\text{O}$ ) 99% purity (J.T. Baker, U.S.), ferric chloride ( $\text{FeCl}_3 \cdot 6\text{H}_2\text{O}$ ) 98% purity (Dinâmica, Brazil), sodium hydroxide (NaOH) 98% purity (Synth, Brazil), microcrystalline cellulose 99% (Synth, Brazil) were used as received. Eucalyptus rafter was acquired from a hardware shop, being milled in a knife mill (Tecnal Te-625) and followed by mechanical classification (200 mesh) to be used as lignocellulosic residues. Distilled water was used for solution preparation.

## Methods

The coprecipitation of IONPs was based on a previous work [6, 15]. Briefly, 4.0 g of  $\text{FeCl}_2 \cdot 4\text{H}_2\text{O}$  and 8.0 g of  $\text{FeCl}_3 \cdot 6\text{H}_2\text{O}$  were dissolved in 150 ml of distilled water, under magnetic stirring and heated at 60 °C, in an open reflux flask. During the dissolution process,  $\text{N}_2$  gas was purged in the solution. Then, a NaOH solution (3 M) was added dropwise until the medium reached pH 12.0. The complete coprecipitation process was carried out in 35 min. The precipitate was then magnetically separated and washed with distilled water until neutral pH. The obtained IONPs were dried at 60 °C for 72 h. For the hybrid's preparation, the coprecipitation was repeated, but with the addition of 6 g (1:0.5), 24 g (1:2), and 96 g (1:8) of microcrystalline cellulose (MC) and 24 g (1:2) of lignocellulosic residue, during the dissolution step. Scheme 1 represents the obtention process.

The size of the IONPs, MC, LR, and hybrids was measured by the dynamic light scattering (DLS) technique using a Zetasizer nano-zs (Malvern Panalytical, US) with a stable 90° scattering angle and a HeNe polarized laser (22 mW) with a wavelength of 633 nm. Samples were diluted to a concentration of 0.01 wt%. Samples morphologies were evaluated using scanning electron microscopy (SEM), model JSM 6010LA, 5 ~ 20 kV (JEOL, Tokyo, Japan). Samples were previously coated with a gold layer, using the sputtering technique (Sputtering Leica ACE200, Wetzlar, Germany). Fourier-transform infrared spectroscopy (FTIR) spectra were recorded using a Frontier 94.942 (PerkinElmer, USA) operating in attenuated total reflectance (ATR) and with a spectral range of 500 to 4000  $\text{cm}^{-1}$ , 64 scans, and a spectral resolution of 4  $\text{cm}^{-1}$ . FTIR Graphs were baseline corrected (25 points) using OriginPro 2018 software. Raman measurements were performed using a confocal micro-Raman spectrometer (T64000, Horiba) with an excitation wavelength of 532 nm and 100X air microscope objective (N.A. 0.60, LUCPlanFLN, Olympus), and its graphs were not baseline corrected. The spectrometer was equipped with a diffraction grating of 1800 gr/mm, which provides a spectral resolution of 0.4  $\text{cm}^{-1}$ . The integration time was set to 2400 s per spectrum, and laser power at the sample was kept about 300  $\mu\text{W}$ . Magnetic measurements were performed using an MPMS from Quantum Design SQUID VSM magnetometer evaluating the hysteresis loops of the IONPs and hybrids. The

**Scheme 1** Simple IONPs and hybrids obtention.



applied field was systematically varied from  $-10.0$  to  $10.0$  kOe. The magnetic susceptibility data were obtained from field-cooling/zero-field cooling (FC/ZFC) curves by heating the sample from  $5$  to  $300$  K with an applied field of  $500$  Oe. First, the sample was cooled down to  $5$  K without any applied field to obtain ZFC measurements; then, the data were obtained after cooling down from  $300$  to  $5$  K with an applied field of  $500$  Oe. The X-ray photoelectron spectroscopy (XPS) analysis was conducted on a ThermoFisher Scientific, model *K-alpha +*, equipped with a monochromatic  $A1 K\alpha$  radiation at  $1486.6$  eV. The analysis was performed at room temperature

and operated at  $10$  or  $20$  eV for high-resolution scans. Data were treated with CASAXPS software.

### Results and discussion

Dynamic light scattering (DLS) was used for the determination of the size of the microcrystalline cellulose (MC), lignocellulosic residues (LR), iron oxide nanoparticles (IONPs), and its hybrids clusters in suspension, and the obtained mean with standard deviation are presented in Fig. 1.

The DLS measures the translational diffusion coefficient of particles in water, which undergo Brownian motion, enabling the determination of particles' average size in suspension [13]. Figure 1 presents the mean values obtained in the DLS measures of the samples. Produced IONPs clusters present a mean value of  $1.57 \mu\text{m}$ , being the lower and the maximum size  $0.93$  and  $2.68 \mu\text{m}$ , respectively, the smaller particles obtained. The best hybrid produced was the IONP + LR  $1:2$ , which remained in sizes between  $1.15$  and  $2.02 \mu\text{m}$ . In comparison, a coprecipitation method applied to synthesize nanomagnetite coated with citric acid produced agglomerated nanoparticles (NPs) with average sizes of  $5.13$ ,  $5.03$ ,  $0.025$ , and  $0.022 \mu\text{m}$ . The authors attributed this effect to the reaction temperature, which was  $65^\circ\text{C}$  [15]. Thus, the size obtained agree with literature reports, and if needed, a homogeneous precipitator could be

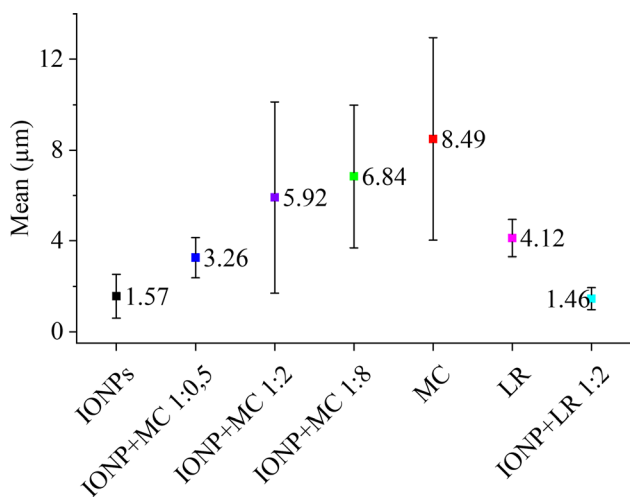


**Figure 1** Size distribution of MC, LR, IONPs, and their hybrids.

used (e.g., urea) to reduce particles' aggregation [2, 15]. Evaluating the MC and LR is possible to observe that they presented larger sizes and wide size distribution. To MC, the sizes varied from 5.86 to 13.64  $\mu\text{m}$ , in agreement with the literature [16] Regarding the LR, DLS analysis showed a particle size between 3.58 and 5.07  $\mu\text{m}$ , also coherent with the observed by the literature [18]. As the IONPs content grows in the produced MC hybrids, the clusters were smaller and presented a narrow distribution. This effect can be attributed to the iron salts amount during the coprecipitation step of the hybrid production. As the iron salts proportion to cellulose matrix is higher, it induces homogeneous precipitation due to the higher deposition area covered. This reduces the effects of the fiber agglomeration, also reducing the whole size of the clusters. Concomitantly, the LR hybrid also presents a smaller cluster size and distribution than the LR matrix. However, the IONPs + LR 1:2 cluster was smaller than IONPs + MC 1:2, which have the same organic and inorganic mass proportion. This indicates that the

organic matrix size also interferes with the final cluster size of the hybrids.

To complement the DLS, the morphological analysis was conducted by scanning electron microscopy (SEM), and Fig. 2 presents images taken from the IONPs, MC, LR, and hybrids. Regarding the IONPs, Fig. 2a shows an irregular morphology due to particle aggregation, which was expected, and the sizes presented similar values to those found by DLS. For the MC and LR, Fig. 2b and 2-c, it is observed that both samples presented a fibril-shaped structure, and the MC presented a more ordered and compact structure, possibly due to the absence of lignin and hemicellulose, both present for the LR matrix. For the hybrids, IONP + MC 1:0.5 (Fig. 2d), 1:2 (Fig. 2e), 1:8 (Fig. 2f), and IONP + LR 1:2 (Fig. 2g) show the matrix fibril character and the presence of crystal deposition at their surface, as highlighted with red circles, which indicates IONPs deposition.

In addition to the SEM images, spot and line energy-dispersive X-ray spectroscopy (EDX) analyses were performed and are presented in Table S1 (Supplementary Material), confirming IONPs presence at the fiber surface.

The obtained Fourier-transform infrared spectroscopy (FT-IR) spectra of the IONPs, MC, LR, and its hybrids are presented in Fig. 3. The full spectra obtained from the 500 to 4000  $\text{cm}^{-1}$  range of the samples are presented in Fig. 3a, where some main peaks were highlighted as vibrational modes of each material used to produce the hybrids. Starting with LR samples, which are made of untreated fibers, is observed a band at 1730  $\text{cm}^{-1}$  associated with carbonyl groups (C=O) that are present in the acetyl ester and carbonyl aldehyde groups of hemicellulose and lignin, whereas the band at 1238  $\text{cm}^{-1}$  refers to -COO vibration mode of acetyl groups in hemicellulose [17–19]. These bands were absent in MC, because this is chemically treated to remove lignin and hemicellulose, and consequently, it is a purified material. On the other hand, the band observed at 1030  $\text{cm}^{-1}$  corresponds to the stretching vibration of the C–O–C antisymmetric (in-phase) pyranose ring, while the peak at 894  $\text{cm}^{-1}$  refers to C–H deformation, typically observed for cellulose structure [17, 18]. Other bands also identified include a broadband at 3400 ~ 2900  $\text{cm}^{-1}$  correlated with stretching of -OH groups of lignin, cellulose, and hemicellulose [2, 5, 17, 18].

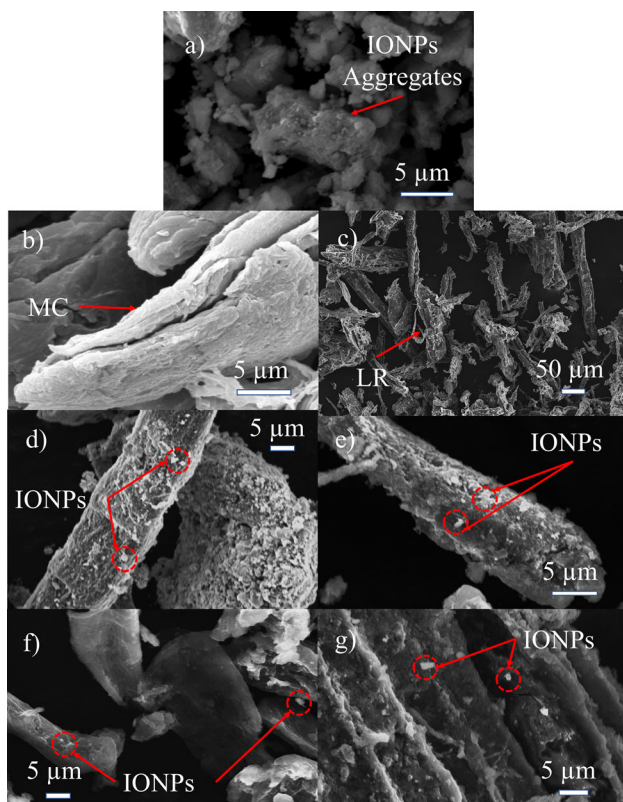


**Figure 2** SEM images MC and LR structures, as well IONPs and hybrids clusters.

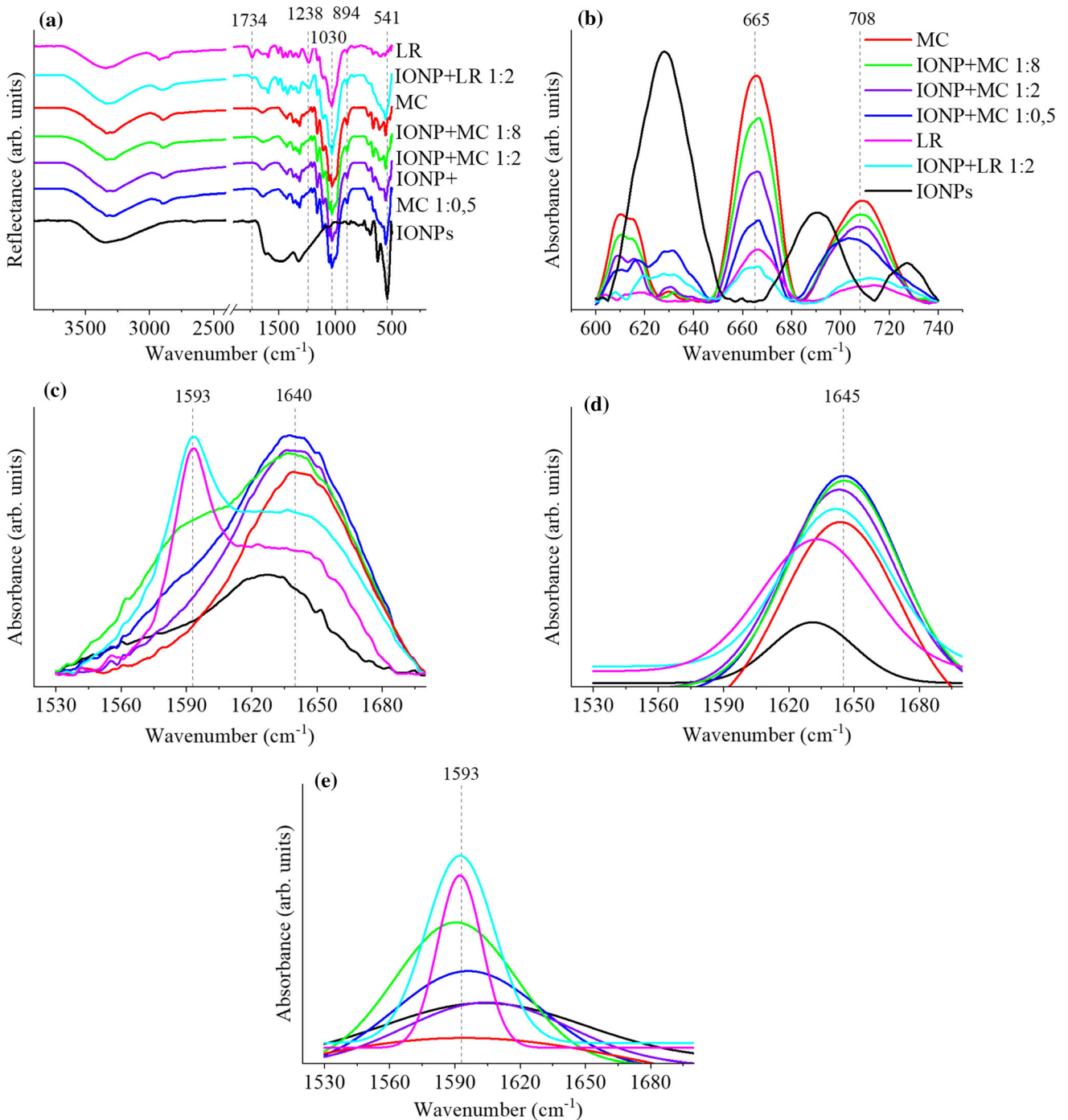


**Figure 3** a FT-IR spectra of IONPs, MC, LR, and the hybrids, b Zoom of the FT-IR spectra from 600 to 740  $\text{cm}^{-1}$  range, c Zoom of the FT-IR spectra from 1530 to 1700  $\text{cm}^{-1}$  range,

d Deconvolution of the sample's spectra at 1593  $\text{cm}^{-1}$ , e Deconvolution of the sample's spectra at 1645  $\text{cm}^{-1}$ .

Regarding the IONPs, the band at 541  $\text{cm}^{-1}$  corresponds to a nonspecific stretching vibration of the Fe–O bound [1]. The IONPs also presented a large band at 3400  $\text{cm}^{-1}$ , suggesting that the oxide material

has water content entrapped in the clusters during the coprecipitation process.

Evaluating the hybrids spectra is possible to observe a similar pattern to those presented by the raw materials. Nevertheless, some distinguish

modifications can be noted as a result of the proportional IONPs deposition. To better understand and evaluation of the hybridization process, the spectra region of 740 to 600  $\text{cm}^{-1}$  was treated and presented in Fig. 3b. A gradual increase in peak 665  $\text{cm}^{-1}$  was observed, from MC and LR spectra to each hybrid, related to IONP content. Kong and Wilson (2017) found that functional groups of goethite ( $\alpha\text{-FeOOH}$ ) nanoparticles and cellulose present a 657  $\text{cm}^{-1}$  band related to Fe–O stretching vibration of goethite while cellulose presented bands for C–OH out-of-plane bending at 662  $\text{cm}^{-1}$  [20]. These findings lead to an understanding that this behavior is due to hydroxides presence in the hybrids. On the other hand, it was observed a reduction at band 708  $\text{cm}^{-1}$ , which is related to the out-of-plane bending mode of C–O–C glycosidic bonds, C(2)–OH, and C(3)–OH groups, and in-plane distortion of armchair rings [21]. Additionally, the region from 1700 to 1520  $\text{cm}^{-1}$  was deconvoluted and is presented in Fig. 3c to Fig. 3e. It is observed from the deconvoluted graph the presence of two main peaks, one at 1593 and the other at 1640  $\text{cm}^{-1}$ . The peak at 1640  $\text{cm}^{-1}$ , presented in Fig. 3d, is associated with the bending modes of water molecule due to a strong interaction between cellulose and water [16] as well as a bending of water interacting with oxide compounds [21, 22]. It was observed that this peak presented an intensity increase for the hybrids when compared to MC, LR, and the IONPs. Additionally, a shift of 5  $\text{cm}^{-1}$  in the deconvoluted peak (from 1640 to 1645  $\text{cm}^{-1}$ ) was observed, suggesting synergic water molecules interaction in the hybrids. The peak at 1593  $\text{cm}^{-1}$ , presented in Fig. 3e, is related to stretching vibrations in aromatic structure C=C, characteristic of lignin softwoods [18]. This peak is absent in MC spectra; however, it presents an intensity increase proportional to IONPs content in each hybrid. Chai and Isa (2012), in their investigations of oleic acid effect on carboxymethyl cellulose (CMC)-based biopolymer electrolyte, identified that the peak COO<sup>-</sup> (1597  $\text{cm}^{-1}$ ) of CMC was less evident with the addition of oleic acid due to a protonation caused by the H<sup>+</sup> cations in the present samples, evidencing the interactions between CMC and oleic acid [23]. These findings corroborate with the previous vibrational stretch modification promoted by the IONPS on the cellulosic materials and are evidence that the hybridization of both cellulosic matrixes was successful.

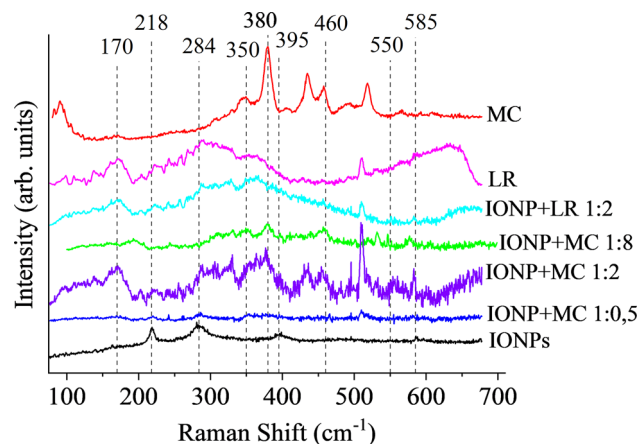


**Figure 4** Micro-Raman spectra of microcrystalline cellulose (MC), lignocellulosic residues (LR), iron oxide nanoparticles (IONPs), and its hybrids.

Micro-Raman analysis was performed to provide evidence of the structures of the raw materials used, the obtained IONPs, and their presence in the hybrids. Figure 4 presents the micro-Raman spectra of MC, LR, IONPs, and their hybrids. Characteristic peaks may be highlighted as assignments of each studied material. Regarding the IONPs structures, spectral regions of 4 iron oxides can be found, as follow: 218 and 284  $\text{cm}^{-1}$  bands, as most distinguished, are related to hematite ( $\alpha\text{-Fe}_2\text{O}_3$ ) phonon modes on A<sub>1g</sub>(1) and E<sub>g</sub>(2) + E<sub>g</sub>(3) vibrational modes; 395  $\text{cm}^{-1}$  band assigned to goethite ( $\alpha\text{-FeOOH}$ ) vibrational mode [24, 25]; 170 and 550  $\text{cm}^{-1}$  bands, both associated with T<sub>2g</sub> vibrational mode of magnetite ( $\text{Fe}_3\text{O}_4$ ) [24, 26, 27]; 585  $\text{cm}^{-1}$  bands related to wustite (FeO), due to an inelastic second harmonic light scattering process [24].

The presence of different iron oxides (IOs) in the same coprecipitate was reported by Salviano et al. (2017), who find magnetite, maghemite, and goethite assignments after two different synthesis conditions for chemical precipitation of magnetite nanoparticles [27]. The literature reports that coprecipitation is a simple method to obtaining magnetic nanoparticles; however, some process steps highly impact the final composition of the produced IONPs. Factors such as hydroxides bulk addition, heat/cooling time, energy transfer by mechanical agitation can influence the IONPs formation kinetics, causing the synthesis and nucleation of more than just one or two different iron oxides, which grows in multiple crystal phases within the other IOs [27, 28]. Regarding MC spectra, the bands at  $\sim 350$ ,  $\sim 380$ , and  $\sim 460$   $\text{cm}^{-1}$  are

related to C–C–C, C–O–C, O–C–C, and O–C–O skeletal bending modes assignments of cellulose structures, along with the C–C–H, and C–O–H groups for the pyranose ring units [17, 29, 30]. These peaks were diminished for IONP + MC 1:2 and 1:0.5 due to maghemite, goethite, and hematite deposition. Regarding LR and IONP + LR 1:2 hybrid spectra, there is a broadband at  $250 \sim 350 \text{ cm}^{-1}$ , related to hemicellulose and lignin in the fibers, and similar peaks at  $\sim 380$  and  $\sim 460 \text{ cm}^{-1}$  associated with cellulose structure. Argarwal et al., (2020) also indicate that bands on  $\sim 490, 503, 522,$  and  $531 \text{ cm}^{-1}$  are related to skeletal deformation of lignocellulosic materials, especially in hardwoods (e.g., *Eucalyptus*) [27]. The IONPS + LR 1:2 hybrid presented an overlapping in bands at  $400 \text{ cm}^{-1}$  and presented peaks in  $218$  and  $284 \text{ cm}^{-1}$  bands due to goethite and hematite deposition. However, there was a less pronounced intensity decrease for  $460 \text{ cm}^{-1}$  band from LR to IONP + LR 1:2 sample, probably because the hemicellulose and lignin, present in the fiber structure, hindered the chemical interaction of cellulose hydroxyl groups with the IONPs. Table S2 (Supplementary Material) presents a summary of the assignments found in the samples.

To evaluate the magnetic response of as-synthesized IONPs, hysteresis loops under different temperatures are presented in Fig. 5. There is no significant difference between the M versus T curves' shape profile at 5 K and 300 K (Fig. 5a and Fig. 5b, respectively).

The obtained data denote that all IONPs systems exhibit fast saturation of magnetization ( $M_s$ ), typical for a superparamagnetic material. The  $M_s$  of the

IONPs-incorporated cellulose matrix ranges from 2 to 15,  $8 \text{ emu g}^{-1}$ , for IONP + MC 1:8 and 1:0.5, respectively, with low remnant magnetization and coercive field at room temperature. The weak hysteresis with a slightly coercive field and saturation magnetization is characteristic of the contribution of soft ferromagnetic material. However, the zero-field-cooled/field-cooled (ZFC/FC) (Fig. 5c) measurements revealed that the 5 over 300 K show a profile characteristic for superparamagnetic behavior [25, 31].

As is well established in the literature, nanosized iron oxides (e.g.: magnetite and maghemite) become superparamagnetic when it reaches a diameter smaller than its critical size [25, 31–33]. This suggests that the dominant superparamagnetic contribution comes from the magnetite nanoparticulated, whereas the discrete ferromagnetic signal comes from other contributions of iron oxide or magnetite with heterogeneous size distribution. Pure cellulosic matrix exhibits negative magnetization as a function of a magnetic field, agreeing with its diamagnetic behavior contributing weakly to the overall magnetic response. The different systems' magnetic response complexity can be explained by the ratio between the amount of cellulosic matrix and magnetite in the composition. Although the IONPs systems showed a decreased  $M_s$  value than IONP, they could still be magnetically separated instantly by an external magnet.

X-ray photoelectron spectroscopy (XPS) analysis allows evaluating the surface electronic state and the atomic composition of the IONPs particles, MC, and LR matrixes, and the hybrids clusters, which are

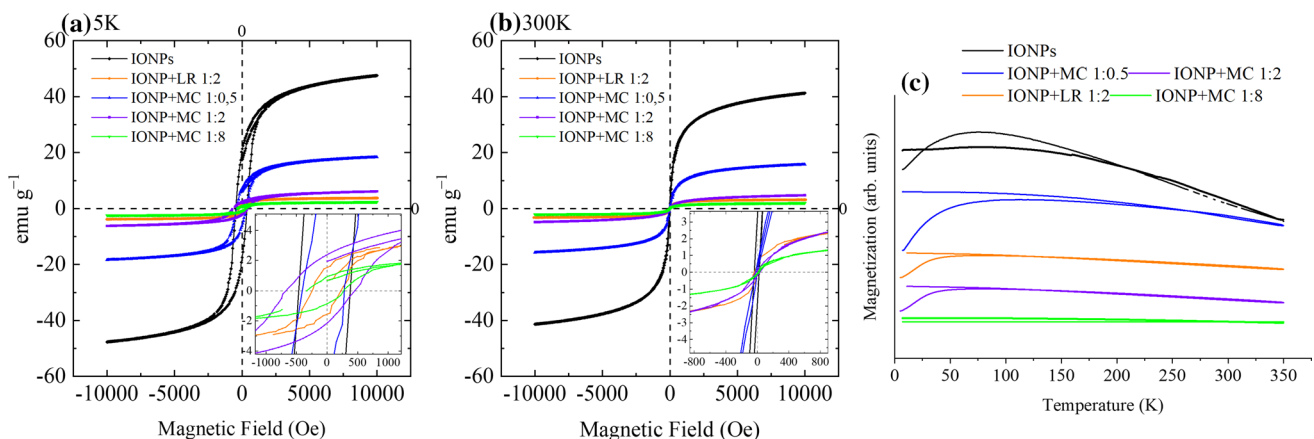


**Figure 5** Magnetization curves of IONPs and their hybrids at temperatures **a** 5 k; **b** 300 k (room temperature); **c** Magnetization x temperature curves of the samples.



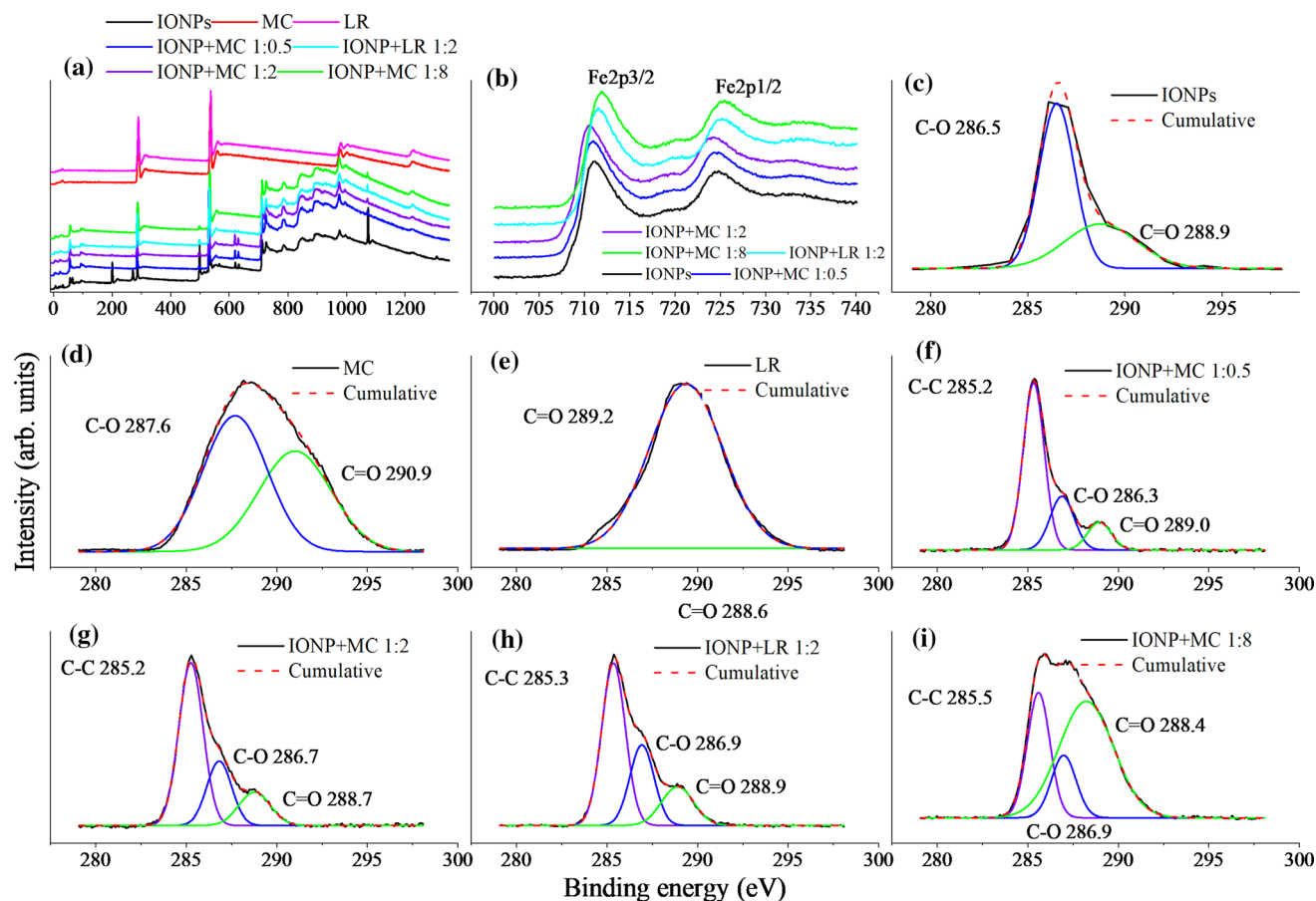


**Figure 6** XPS spectra of IONPs, MC, LR, and the hybrids, where **a** Survey spectra of the samples; **b** Fe2p spectra of IONPs and hybrids; **c** to **i** Gaussian C1s spectra of the samples.

presented in Fig. 6. Figure 6a presents the full-scanning XPS spectrum in the range from 0 to 1400 eV, and it is observed that the hybrids presented a mixed spectrum from the IONPs and LR or MC. The atomic composition evaluation considered carbon, oxygen, and iron species, and the relevant regions are also presented in Fig. 6a. XPS spectrum also reveals the presence of Na (1073.2 eV) and Cl (270.1 eV) at the IONPs sample surface. Sodium chlorides occur as neutralization residue in the produced materials, which was not cared out with the post-precipitation washes. MC and LR present cellulosic features since XPS survey spectra showed the representative C 1s (288.1 and 229.4 eV) and O 1s (534.6 and 537.1 eV) photoemission peaks dominance, which are in agreement with the literature [16, 33]. IONPs present characteristic broad peaks at binding energies (Fig. 6b) of 711.09 and 724.81 eV related to doublets of Fe2p1/2 and Fe2p3/2 spectrum characteristics of Fe<sup>2+</sup> and Fe<sup>3+</sup>, respectively [1, 12, 34].

Gaussian distributions were employed to highlight the C1s bounds in MC, LR, IONPs, and hybrids surface, presented from Fig. 6c to 6i. XPS spectrum of C1s peaks at 286 ~ 287, 288 ~ 289 eV is due to the oxygenated group attached to the carbon atom, such as C–O and C=O groups, respectively, as well as the peak at ~ 285 eV represents the C–C bonds [12, 13]. The presence of carbon in IONPs (Fig. 6c) results from CO<sub>2</sub> contamination from the atmosphere [35]. MC XPS spectra (Fig. 6d) showed mainly C–O, due to the high amount of hydroxyl groups in the cellulose molecules' boundaries, as well as presented C=O binding energies. In contrast, LR spectra (Fig. 6e) presented almost only C=O linkages on their surface due to lignin and hemicellulose presence. On the other hand, hybrids XPS C1s spectra (Fig. 6f, g, h, and i) presented binding energies of C–C, C–O, and C=O bounds. The C–C binding energy presence only in hybrids' surface rather than in MC and LR surfaces draws attention, drawing light on a correlation

between IONPs deposition and binding at cellulosic matrixes.

Cellulose and cellulosic materials are known to make hydrogen bonds due to hydroxyl groups' presence on their boundaries. Thus, interactions of the IONPs and cellulosic material may occur between the oxygen atoms of the iron oxides and the polar -OH groups of cellulose [36], which forms weak hydrogen-bonds, due to the polarization of the  $\pi$ -system, which acts as a proton acceptor [37]. XPS analysis of the C–C binding energy in IONPs-cellulosic 1:0.5 and 1:2 hybrids (Fig. 6f, g and h) against IONP + MC 1:8 (Fig. 6i) is an indication that as much the cellulosic structures are covered with IONPs, lower was the signal strength of the C–O and C=O binding. Therefore, the deposition of the iron oxide nanoparticles in the cellulosic matrixes surface covers the C–O and C=O bonds, leading to an increase in the C–C bond signal. Additionally, IONP + LR 1:2 (Fig. 6-h) presented a more preminent C=O signal than IONP + MC 1:2 (Fig. 6g). This evidence corroborates with the magnetization findings presented above, since IONP + LR 1:2 form fewer hydrogen interactions than IONP + MC 1:2, due a less available hydroxyl groups. Tables S3 and S4 (Supplementary Material) provide a Pearson correlation between the graph's areas of the C–C binding energies, which also corroborates with the discussion above. Scheme 2 summarizes the results presented in this work, showing the difference between the nanosized iron oxides clusters and the cellulosic structures clusters. After their formation, IOs nanocrystals tend to assemble into submicron dimensions clusters [8] through dipolar–dipolar interactions [9], while in the presence of cellulosic

matrix and acid medium, the newly formed iron nanoparticles are attracted by the protonated polar hydroxyl groups of the cellulose, forming hydrogen bonds.

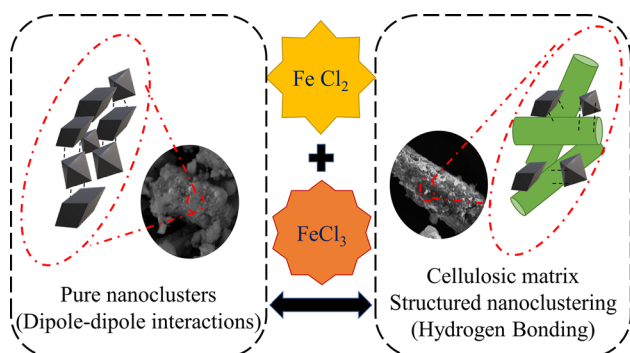
Thus, the coprecipitation process applied produced heterogeneous iron oxide nanosized crystals, which was hydrogen bonded to the cellulosic or lignocellulosic organic backbone microstructures. As the cellulosic clusters obtained kept superparamagnetic properties despite the organic fraction of the hybrids, the produced material keeps interesting features for a whole different application.

## Conclusion

This work provided evidence of linkage by hydrogen bond between iron oxide nanoparticles and microcrystalline cellulose and lignocellulosic residues, obtained through coprecipitation. Different characterization techniques were applied to prove the size, morphology, chemical structures, and bound of the obtained nanoclusters. The IONPs deposition was visible on SEM images, and magnetization shows that all synthesized clusters presented superparamagnetic behavior at room temperature, which confirms the nanoscale of the IONPs hybrids, despite the organic fraction. Also, FTIR, micro-Raman, and XPS data indicated by many means that hydroxyl groups of the cellulosic matrix form the hydrogen bonds with the IONPs. Thus, a simple and easy-to-reproduce nanoclustering process was applied to obtain heterogeneous SPM metal–organic hybrids, avoiding the use of surfactants or surface modifying agents, working both for pure cellulose and lignocellulosic residues, expanding IONPs application using low-cost process and materials.

## Acknowledgements

The authors would like to thank FAPESP (Fundação de Amparo à Pesquisa do Estado de São Paulo) project number 2018/11277-7; CNPq (Conselho Nacional de Desenvolvimento Científico e Tecnológico), Project number 305819/2017-8 and CAPES (Coordenação de Aperfeiçoamento de Pessoal de Nível Superior) for the support with scholarship.



**Scheme 2** Comparison between pure IONPs nanoclusters and their dipole–dipole interactions against cellulosic matrix structured nanoclustering and its hydrogen bonding.

## Author contributions

The manuscript was written through the contributions of all authors.

## Declarations

**Conflict of interest** The authors declare that they have no known competing financial interests or personal relationships that could have appeared to influence the work reported in this paper.

**Human or animal rights** This study does not contain any studies with human participants or animals performed by any of the authors.

**Informed consent** For this type of study, formal consent is not required.

**Associated content** Energy-dispersive X-ray spectroscopy (EDX) and Micro-Raman assignments of the samples, as well as Pearson correlation between the C–C binding energies of the hybrids, are included in this work as Supplementary Material.

**Supplementary Information:** The online version contains supplementary material available at <http://doi.org/10.1007/s10853-021-06564-z>.

## References

- [1] Chaabane L et al (2020) Functionalization of developed bacterial cellulose with magnetite nanoparticles for nanobiotechnology and nanomedicine applications. *Carbohydr Polym* 247:116707–116719. <https://doi.org/10.1016/j.carbpol.2020.116707>
- [2] Damodaran P (2020) Mesoporous magnetite nanoclusters as efficient nanocarriers for paclitaxel delivery. *Chem Sel* 5(29):9261–9268. <https://doi.org/10.1002/slct.202001102>
- [3] Ganesan V, Louis C, Damodaran SP (2018) Novel nanofluids based on magnetite nanoclusters and investigation on their cluster size-dependent thermal conductivity. *T J Phys Chem C* 122(12):6918–6929. <https://doi.org/10.1021/acs.jpcc.7b12043>
- [4] Seabra AB, Pelegrino MT, Haddad PS (2017) Antimicrobial applications of Superparamagnetic iron oxide nanoparticles: perspectives and challenges. *Nanostruct Antimicrob Ther*. <https://doi.org/10.1016/B978-0-323-46152-8.00024-X>
- [5] Arantes ACC et al (2017) Renewable hybrid nanocatalyst from magnetite and cellulose for treatment of textile effluents. *Carbohydr Polym* 163:101–107. <https://doi.org/10.1016/j.carbpol.2017.01.007>
- [6] Zhareif S, Niad M, Raanaei H (2018) The removal of mercury ion pollution by using Fe<sub>3</sub>O<sub>4</sub>-nanocellulose: synthesis, characterization and DFT studies. *J Hazard Mater* 344:258–273. <https://doi.org/10.1016/j.jhazmat.2017.10.009>
- [7] Kaco H et al (2017) Preparation and characterization of Fe<sub>3</sub>O<sub>4</sub>/regenerated cellulose membrane. *Sains Malays* 46(4):623–628. <https://doi.org/10.17576/jsm-2017-4604-15>
- [8] Ganesan V et al (2019) Size-controlled synthesis of superparamagnetic magnetite nanoclusters for heat generation in an alternating magnetic field. *J Mol Liquids* 281:315–323. <https://doi.org/10.1016/j.molliq.2019.02.095>
- [9] Manh-Huong P et al (2016) Exchange bias effects in iron oxide-based nanoparticle systems. *Nanomaterials* 6(11):221–251. <https://doi.org/10.3390/nano6110221>
- [10] Mohamed MA et al (2017) An overview on cellulose-based material in tailoring bio-hybrid nanostructured photocatalysts for water treatment and renewable energy applications. *Int J Biol Macromol* 103:1232–1256. <https://doi.org/10.1016/j.ijbiomac.2017.05.181>
- [11] Gharibshahi R et al (2020) Hybridization of superparamagnetic Fe<sub>3</sub>O<sub>4</sub> nanoparticles with MWCNTs and effect of surface modification on electromagnetic heating process efficiency: a microfluidics enhanced oil recovery study. *Fuel* 282:118603–118617. <https://doi.org/10.1016/j.fuel.2020.118603>
- [12] Benjwal P et al (2015) Enhanced photocatalytic degradation of methylene blue and adsorption of arsenic (iii) by reduced gra-phene oxide (rGO)–metal oxide (TiO<sub>2</sub>/Fe<sub>3</sub>O<sub>4</sub>) based nanocomposites. *Rsc Adv* 5(89):73249–73260. <https://doi.org/10.1039/C5RA13689J>
- [13] Lian Z et al (2020) EDTA-functionalized magnetic chitosan oligosaccharide and carboxymethyl cellulose nanocomposite: synthesis, characterization, and Pb (II) adsorption performance. *Inter J Biol Macromol* 165:591–600. <https://doi.org/10.1016/j.ijbiomac.2020.09.156>
- [14] Abouzeid RE et al (2018) Current state and new trends in the use of cellulose nanomaterials for wastewater treatment. *Biomacromol* 20(2):573–597. <https://doi.org/10.1021/acs.biomac.8b00839>
- [15] Dheyab MA et al (2020) Simple rapid stabilization method through citric acid modification for magnetite nanoparticles. *Sci Rep* 10(1):1–8. <https://doi.org/10.1038/s41598-020-67869-8>
- [16] Souza AG et al (2019) A new approach for conversion of eucalyptus lignocellulosic biomass into cellulose nanostructures: a method that can be applied in industry. *J Nat Fibers*. <https://doi.org/10.1080/15440478.2019.1691125>

- [17] Ferreira RR et al (2019) Use of ball mill to prepare nanocellulose from eucalyptus biomass: challenges and process optimization by combined method. *Mater Today Commun* 22:100755–100768. <https://doi.org/10.1016/j.mtc.omm.2019.100755>
- [18] de Souza AG et al (2019) Valorization of industrial paper waste by isolating cellulose nanostructures with different pretreatment methods. *Resour. Conserv Recycl* 143:133–142. <https://doi.org/10.1016/j.resconrec.2018.12.031>
- [19] Moosavinejad SM et al (2019) Evaluation of degradation in chemical compounds of wood in historical buildings using FT-IR and FT-Raman vibrational spectroscopy. *Maderas Cienc Tecnol* 21(3):381–392. <https://doi.org/10.4067/S0718-221X2019005000310>
- [20] Kong D, Wilson LD (2017) Synthesis and characterization of cellulose-goethite composites and their adsorption properties with roxarsone. *Carbohydr Polym* 169:282–294. <https://doi.org/10.1016/j.carbpol.2017.04.019>
- [21] Makarem M et al (2019) Probing cellulose structures with vibrational spectroscopy. *Cellul* 26(1):35–79
- [22] Sergeeva AV et al (2020) Infrared and Raman spectroscopy of ammoniovoltaite,  $(\text{NH}_4)_2\text{Fe}^{2+}_5\text{Fe}^{3+}_3\text{Al}(\text{SO}_4)_{12}(\text{H}_2\text{O})_{18}$ . *Miner* 10(9):781–795. <https://doi.org/10.3390/min10090781>
- [23] Chai MN, Isa MIN (2013) The oleic acid composition effect on the carboxymethyl cellulose based biopolymer electrolyte. *J Cryst Process Tech* 3(1) 1–4. <http://www.scirp.org/journal/PaperInformation.aspx?PaperID=27263>
- [24] Testa-Anta M et al (2019) Raman spectroscopy to unravel the magnetic properties of iron oxide nanocrystals for bio-related applications. *Nanoscale Adv* 1(6):2086–2103. <https://doi.org/10.1039/C9NA00064J>
- [25] Williams GVM et al (2018) Spin-dependent tunnelling in magnetite nanoparticles. *J Magn Magn Mater* 460:229–233. <https://doi.org/10.1016/j.jmmm.2018.04.017>
- [26] Kumar CSSR (2012) Raman spectroscopy for nano-materials characterization. *Springer Sci Bus Media*. <https://doi.org/10.1007/978-3-642-20620-7>
- [27] Salviano LB et al (2018) Microstructural assessment of magnetite nanoparticles ( $\text{Fe}_3\text{O}_4$ ) obtained by chemical precipitation under different synthesis conditions. *Mater Res* 21(2):764–771. <https://doi.org/10.1590/1980-5373-mr-2017-0764>
- [28] Wroblewski C et al (2020) High yield synthesis and application of magnetite nanoparticles ( $\text{Fe}_3\text{O}_4$ ). *Magnetochem* 6(2):22–34. <https://doi.org/10.3390/magnetochemistry6020022>
- [29] Agarwal UP, McSweeney JD, Ralph SA (2011) FT-Raman investigation of milled-wood lignins: softwood, hardwood, and chemically modified black spruce lignins. *J Wood Chem Tech* 31(4):324–344. <https://doi.org/10.1080/02773813.2011.562338>
- [30] Kong D, Wilson LD (2018) Structural study of cellulose-iron oxide composite materials. *J Mater Sci Chem Eng* 6(4):65–77. <https://doi.org/10.4236/msce.2018.64009>
- [31] Furlan DM et al (2019) Sisal cellulose and magnetite nanoparticles: formation and properties of magnetic hybrid films. *J Mater Res Tech* 8(2):2170–2179. <https://doi.org/10.1016/j.jmrt.2019.02.005>
- [32] Francisquini, E., Schoenmaker, J., Souza, J.A., (2014) Nanopartículas magnéticas e suas aplicações. *Qum. Supramol, Nano-tecnol., Atheneu* 269
- [33] Maccarini M et al (2014) Interactions at the CMC/magnetite interface: implications for the stability of aqueous dispersions and the magnetic properties of magnetite nanoparticles. *Colloids Surf A: Physicochem Eng Asp* 462:107–114. <https://doi.org/10.1016/j.colsurfa.2014.08.026>
- [34] Guo J et al (2017) Complexes of magnetic nanoparticles with cellulose nanocrystals as regenerable, highly efficient, and selective platform for protein separation. *Biomacromol* 18(3):898–905. <https://doi.org/10.1021/acs.biomac.6b01778>
- [35] Carvalho-Jr WM et al (2019) Annealing control of hydrothermally grown hematite nanorods: implication of structural changes and Cl concentration on weak ferromagnetism. *J Alloys Compd* 799:83–88. <https://doi.org/10.1016/j.jallcom.2019.05.335>
- [36] Chauhan I et al (2019) Immobilization of  $\alpha\text{-Fe}_2\text{O}_3$  nanoparticles on the cellulose surface: role of cellulose in tuning the microstructure and crystallographic phase. *Cellul* 26(3):1757–1767. <https://doi.org/10.1007/s10570-018-2186-4>
- [37] Dzade NY, Roldan A, Leeuw NH (2014) A density functional theory study of the adsorption of benzene on hematite ( $\alpha\text{-Fe}_2\text{O}_3$ ) surfaces. *Miner* 4(1):89–115. <https://doi.org/10.3390/min4010089>

**Publisher's Note** Springer Nature remains neutral with regard to jurisdictional claims in published maps and institutional affiliations.